DNA tensiometer reveals catch-bond detachment kinetics of kinesin-1, -2 and -3

Crystal R. Noell[1], Tzu-Chen Ma[1], Rui Jiang[1], Scott A. McKinley[2], William O. Hancock*[1,3]

[1] Department of Biomedical Engineering, Pennsylvania State University, University Park, Pennsylvania, USA
[2] Department of Mathematics, Tulane University, New Orleans, Louisiana, USA
[3] Department of Chemistry, Pennsylvania State University, University Park, Pennsylvania, USA

* Corresponding author
Email: woh1@psu.edu

Author Contributions: S.A.M. and W.O.H. conceived of original idea, C.R.N., R.J. and W.O.H. designed research; C.R.N., R.J. and T.M. performed research; C.R.N., T.M. and S.A.M. analyzed data; C.R.N., T.M., S.A.M., and W.O.H. wrote the paper.
Competing Interest Statement: The authors declare that they have no known competing financial interests or personal relationships that could have appeared to influence the work reported in this paper.
Keywords: Kinesin, intracellular transport, molecular mechanics, molecular machine, mechanochemistry

Abstract

Bidirectional cargo transport by kinesin and dynein is essential for cell viability and defects are linked to neurodegenerative diseases. Computational modeling suggests that the load-dependent off-rate is the strongest determinant of which motor 'wins' a kinesin-dynein tug-of-war, and optical tweezer experiments find family-dependent differences in the sensitivity of detachment to load, with kinesin-3 > kinesin-2 > kinesin-1. However, in reconstituted kinesin-dynein pairs vitro, all three kinesin families compete nearly equally well against dynein. Modeling and experiments have confirmed that vertical forces inherent to the large trapping beads enhance kinesin-1 dissociation rates. In vivo, vertical forces are expected to range from negligible to dominant, depending on cargo and microtubule geometries. To investigate the detachment and reattachment kinetics of kinesin-1, 2 and 3 motors against loads oriented parallel to the microtubule, we created a DNA tensiometer comprising a DNA entropic spring attached to the microtubule on one end and a motor on the other. Kinesin dissociation rates at stall were slower than detachment rates during unloaded runs, and the complex reattachment kinetics were consistent with a weakly-bound 'slip' state preceding detachment. Kinesin-3 behaviors under load suggested that long KIF1A run lengths result from the concatenation of multiple short runs connected by diffusive episodes. Stochastic simulations were able to recapitulate the load-dependent detachment and reattachment kinetics for all three motors and provide direct comparison of key transition rates between families. These results provide insight into how kinesin-1, -2 and -3 families transport cargo in complex cellular geometries and compete against dynein during bidirectional transport.

Introduction

Bidirectional cargo transport by kinesin and dynein motors is essential for cell viability, and disruptions in transport are linked to neurological diseases including hereditary spastic paraplegia, microcephaly and amyotrophic lateral sclerosis [1-8]. It has been established that kinesin and dynein, which move in opposite directions along microtubules, are often bound simultaneously to the same cargo [9-12]. This has led to the 'tug-of-war' model, in which the direction of cargo movement is determined by which team of motors dominates [9,13-17]. How well motors compete is determined by their load-dependent motor properties along with multiple regulation mechanisms, many of which are still emerging [13,18-21]. Furthermore, the large range of cargo sizes and the complexity of microtubule organization in cells means that motors are subjected to forces both parallel and perpendicular to their microtubule track, which can have differing effects on their mechanochemistry.

Intuitively, a motor's effectiveness in transporting cargo rests on its ability to remain bound to its microtubule track. Consistent with this, computational simulations have found that the load-dependent off-rate of a motor is the most important determinant of how well a kinesin competes against dynein in bidirectional transport [22,23]. Single-bead optical tweezers have found that the transport motors kinesin-1, -2, and -3 all act as slip bonds, defined as load accelerating their detachment rate. Their propensity to detach under load varies strongly by family, with relative load sensitivity kinesin-3 > kinesin-2 > kinesin-1 [24-27]. Based on this behavior, it was surprising that when kinesin-1 was linked to dynein, complexes moved at near-zero speeds for up to tens of seconds, much longer than predicted based on previously measured kinesin-1 off-rates [25,28,29]. Moreover, kinesin-1, -2, and -3 all fared equally well against dynein, contrary to the differing load-dependent detachment rates measured in single-bead optical tweezer experiments [30].

Recent work suggests a solution to this paradox, namely that the ~micron scale beads used for optical trapping result in significant forces oriented perpendicular to the microtubule as the motor pulls against the force of the trap. First, the load-dependent dissociation rate from single-bead optical trapping was accounted for by a model in which the effects of horizontal loads on detachment is highly asymmetric and vertical loads play a dominant role in detachment, particularly against hindering loads [31]. Second, when a three-bead optical trapping geometry was used (in which the motor is raised up on a pedestal bead and the microtubule was held by beads attached to either end of the microtubule) motors remained bound longer than in the single-bead geometry [24,32]. Third, when kinesin-1 motors were connected to a microtubule by a micron-long segment of DNA, very long residence times were observed, consistent with catch-bond behavior, defined as the off-rate slowing with load [33]. Fourth, when kinesin-1 was connected to a bead through a micron-long segment of DNA and hydrodynamic forces were imposed on the bead, motor interaction times were insensitive to hindering loads up to 3 pN, indicative of an ideal-bond [34]. In cells, kinesin and dynein transport cargoes that range from tens of nm in diameter (like vesicles), where motor forces are expected to be aligned parallel to the microtubule, up to several microns (like mitochondria and nuclei), where vertical forces are expected to be much larger. Thus, understanding the influence of vertical and horizontal forces on transport motors is important for understanding the mechanics underlying bidirectional transport in cells.

The goal of the present study was to characterize the load-dependent detachment kinetics of kinesin-1, -2 and -3 motors in a geometry that eliminates vertical forces inherent in traditional optical trapping studies. Building on previous approaches, we used double stranded DNA (dsDNA), which acts as an entropic spring to resist the pN-level forces generated by the motors [33-38]. We found that kinesin-1, -2, and -3 all remained at stall for multiple seconds before releasing, durations that are substantially longer than the unloaded run times for kinesin-1 and -2. This behavior of slower off-rates under load is defined as a 'catch bond', and contrasts with the normal 'slip bond' behavior load-accelerated off-rates generally observed for kinesin [25,39,40]. Following the termination of a stall, motors reengaged with the microtubule with complex kinetics that were consistent with a 'slip' state that preceded full detachment. To compare the key transition rates that determined the family-specific motor behaviors, we developed a stochastic model that was able to recapitulate the experimental results for all three motors.

Results

Constructing a motor-bound DNA tensiometer

To study motor performance against a resistive load oriented parallel to the microtubule, we constructed a DNA tensiometer consisting of a ~ 1 μm strand of dsDNA attached to the microtubule on one end and a motor on the other (Figure 1A). We used TIRF microscopy to visualize the motor moving against the entropic elasticity of the DNA spring. Due to the nonlinear elasticity of the DNA (Figure 1B) [35,36], the motor moves under minimal load until it stretches the DNA to near its contour length, at which point it stalls (Figure 1C-E).

Our DNA-motor tensiometer consists of a 3,009 bp (999 nm contour length) dsDNA 'spring' that was synthesized by PCR using a biotinylated forward primer for attachment to the microtubule and a reverse primer containing a 3' overhang for motor attachment (details in Methods). We investigated members of the three dominant families of kinesin transport motors, kinesin-1 (*Drosophila melanogaster* KHC), kinesin-2 (*Mus musculus* Kif3A), and kinesin-3 (*Rattus norvegicus* Kif1A) used in our previous kinesin-dynein study [30]. In each case, the motor and neck linker domains were fused to the stable neck-coil domain (residues 345-406) of kinesin-1, followed by EGFP, a SNAP tag, and His_6 tag, as described previously [30]. This dimerization strategy avoids any autoinhibition and family-dependent differences in neck-coil stability, thus enabling the most direct comparison of family-dependent motor properties. Motors were conjugated to an oligonucleotide complimentary to the 3' overhang of the dsDNA spring via their C-terminal SNAP tag. The DNA tensiometer complex (Figure 1A) was created in a flow cell by sequentially flowing in biotinylated microtubules, neutravidin, biotinylated dsDNA, and Qdot-functionalized motors containing the complimentary oligo (described fully in Methods).

The resulting dsDNA tensiometer kymographs (Figure 1C) show a reproducible behavior of moving, stalling, and returning to origin multiple times, which contrasts with the singular attachment, unidirectional movement and detachment of motors not bound by DNA (Figure S1). Because motors are tethered to the microtubule by the flexible DNA, large fluctuations around the origin are observed when the motor is detached

(Figure 1C-H). Consistent with these fluctuations, initial attachment points were variable and roughly normally distributed with a standard deviation of 145 nm (Figure S2). Upon engagement with the microtubule, the motor walks at a steady velocity, consistent with the expected nonlinear stiffness of the dsDNA tether (Figure 1B), until it either disengages or reaches a stall state. Stalls are terminated either by the motor slipping backwards a short distance and restarting a new ramp, or by the motor fully disengaging and returning to the baseline (Figure 1E-H and Figure S3). To confirm that motors are indeed extending the DNA and that Qdots are not enabling multi-motor assemblies, we incorporated Cy5-dCTP into the dsDNA and left the Qdots out of the reaction. In this case, clear extensions of the DNA spring could be observed, and the stall durations were of similar duration (Figure S4). In all subsequent experiments dsDNA was labeled with a low concentration of Cy5-dCTP to confirm colocalization of the DNA and the microtubule before collecting tensiometer data.

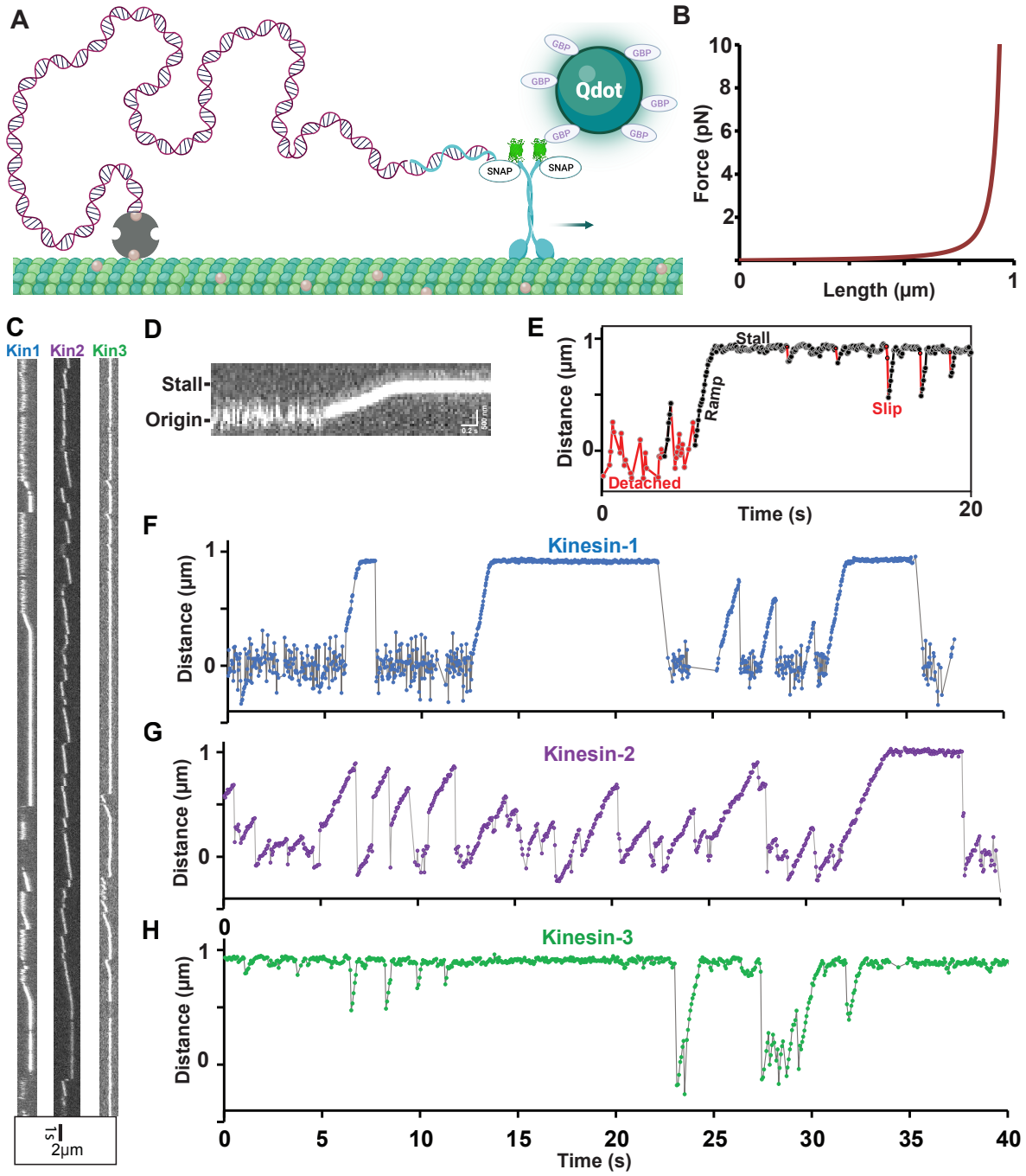

Figure 1. Experimental Design and Raw Data from Motor-DNA Tensiometers. (A) Schematic of a motor-DNA tensiometer, consisting of a dsDNA (burgundy) connected on one end to a kinesin motor through a complimentary oligo (blue), and on the other end to the MT using biotin-avidin (tan and gray, respectively). A Qdot functionalized with GFP binding protein nanobodies is attached to the motor's GFP tag and used to track motor position. (Not to scale; motor and Qdot are both ~20 nm and DNA is ~1 micron) (B) Predicted force extension curve for a worm-like chain 3009 bp dsDNA based on a 50 nm persistence length. (C) Representative kymographs of motor-DNA tensiometers for kinesins-1, -2 and -3. (D) Enlarged kymograph showing diffusion around the origin, ramp, and stall. (E) Example distance vs.

time trace (kinesin-3), highlighting detached durations (red), ramps and stalls (black) where the motor has pulled the DNA taut, and transient slips during stall (red). (F-H) Representative distance vs. time plots for kinesin-1 (F), kinesin-2 (G) and kinesin-3 (H), corresponding to the kymographs in (C). Further examples are shown in Figure S3.

Kinesin-1 and -2 act as catch-bonds at stall

The first question we addressed was: what are the detachment rates of kinesin-1, -2 and -3 motors at stall? The load-dependence of protein-protein interactions can be described as a slip-bond [41], defined as a faster off-rate under load; an ideal bond, defined as an off-rate that is independent of load; or a catch-bond, in which the off-rate is slower under load [39]. Single-bead optical trapping studies consistently find slip-bond characteristics for kinesin-1, 2 and 3 [25,27,42], whereas dynein off-rates have been described as a slip-bond or catch-bond [43-46].

We define stall duration as the time that a motor stalls against the hindering load of fully extended DNA, without further detectable stepping. Stalls are terminated by the motor detectably (>60 nm) slipping backwards or by disengaging and returning to the origin (Figure 1E). Although we don't directly measure the stall force, based on the predicted force-extension curve of the dsDNA (Figure 1B), the displacements are consistent with the 4-6 pN stall forces for kinesin-1, -2 and -3 measured using optical traps [27,47-51]. Stall durations were compared to the unloaded single-motor run durations determined from TIRF kymograph analysis (Figure S1).

To compare unloaded off-rates to off-rates at stall, cumulative distributions of the run and stall durations were plotted for each motor and fit with a single exponential function (Figure 2). The kinesin-1 tensiometer stall duration time constant was 3.01 s, with 95% confidence intervals (CI) of 2.30 to 3.79 s determined via bootstrapping in MEMLET [52] with 1000 iterations (N= 78 stalls). In contrast, the kinesin-1 unloaded run duration time constant, measured by a traditional TIRF assay, was 1.04 s, (Figure 2A; Table S1). Stall durations longer than unloaded run durations indicate that load slows the off-rate, the definition of a catch-bond [39]. Similarly, the kinesin-2 tensiometer stall duration time constant of 2.83 s was longer than its unloaded run duration of 1.07 s, also indicating a catch-bond (Figure 2B). Conversely, the kinesin-3 tensiometer stall duration time constant of 1.89 s was shorter than its unloaded run duration of 2.74 s, indicating a slip-bond characteristic by this definition.

We carried out two additional control experiments. First, to confirm that the neutravidin used to link the DNA to the microtubule wasn't affecting kinesin motility, we analyzed the run durations of kinesin-1 motors on neutravidin-coated microtubules and found no significant change in the unloaded run duration (Fig. S6). Second, we measured the run duration of kinesin-1 linked to a DNA tether that was not bound to the microtubule and thus was being transported (Fig. S6). The kinesin-DNA run duration was 1.40 s, longer than the 1.04 s of motors alone (Fig. 2A). We interpret this longer duration to reflect the slower diffusion constant of the dsDNA relative to the motor alone, which enables motors to transiently detach and rebind before the DNA cargo has diffused away, thus extending the run duration [53]. Notably, this slower diffusion constant should not play a role in the DNA tensiometer geometry because if the motor transiently detaches, it will be pulled backward by the elastic forces of the DNA and detected as a slip or detachment event.

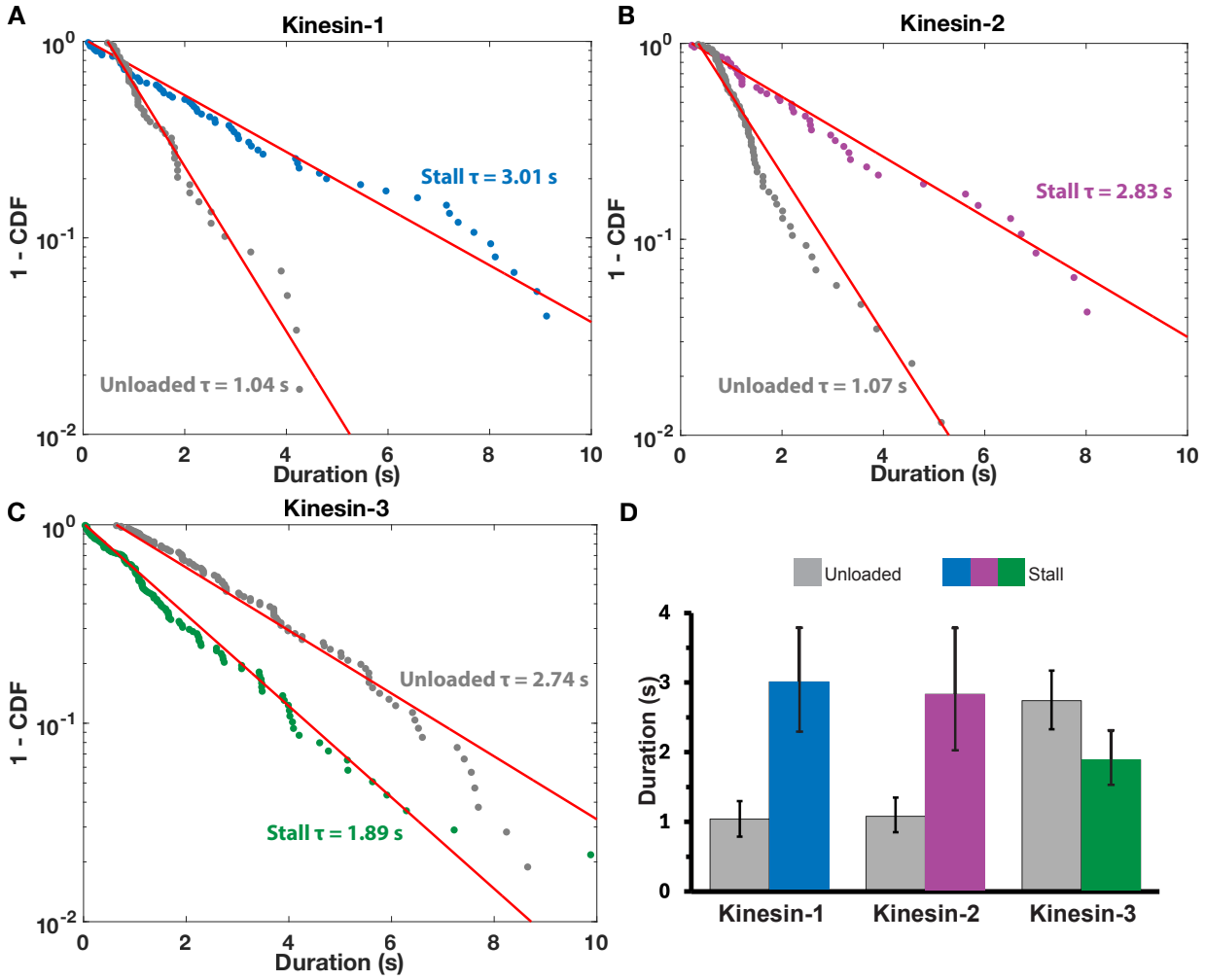

Figure 2. Tensiometer Stall Durations Indicate Catch-bond Behavior for Kinesin-1 and -2. Tensiometer stall durations are plotted for (A) kinesin-1 (blue), (B) kinesin-2 (purple), and (C) kinesin-3 (green). Unloaded run durations for each motor are plotted in gray. Distributions were fit with a single exponential function using MEMLET to generate time constants, representing the mean durations. (D) Comparison of unloaded and stall durations for the three motors, with error bars indicating 95% CI. Stall durations >20s were excluded from the fit (three events for kinesin-1 and two events for kinesin-2). All fit parameters are given in Table S1 and bi-exponential fits of all data including >20 s are shown in Figure S5.

Kinesin-3 detaches readily under low load

To determine whether sub-stall hindering loads affect motor detachment rates, we compared tensiometer ramp durations to the tensiometer stall and unloaded run durations (Figure 3). We defined ramp durations as the time the motor spends walking against the DNA spring before a slip or detachment, or before reaching stall. Although the dsDNA force-extension curve (Figure 1B) predicts negligible loads until the DNA is close to fully extended, there are still non-zero loads imposed during the ramp phase that may affect motor detachment. Based on 10-20% slower ramp velocities relative to unloaded velocities for each motor, we estimated the apparent force to be ~1 pN (Table

S2). To estimate the true detachment rate during the ramp phase in a way that takes into account both the observed detachments and ramps that successfully reach stall, we used a Markov process model, coupled with Bayesian inference methods (detailed in Supplementary Material) to estimate a duration parameter, τ, equivalent to the inverse of the detachment rate constant during a ramp. Each increment of time is considered to be an independent opportunity to detach while assuming a constant detachment rate; hence the probability of staying attached to the microtubule through a segment of duration Δ is $e^{-\Delta/\tau}$. Using this method, ramp duration parameters, τ, were calculated for each motor, along with 95% credible regions. Finally, to allow for proper comparison, we performed a similar analysis to obtain the stall and unloaded duration parameters along with their 95% credible regions (Figure 3). As expected, the stall and unloaded durations were similar to estimates from curve fitting in Figure 2 (Table S1).

The prediction for a slip bond is that against the low loads experienced during ramps, the detachment rate should be equal to or faster than the unloaded detachment rate. This was the case for kinesin-2, where the ramp duration of 0.97 s was within 95% CI of the unloaded run duration of 1.08 s (Figure 3B, Table S1). In contrast, the kinesin-1 ramp duration of 2.49 s was much closer to the stall duration (3.05 s) than the unloaded run duration (1.05 s) (Figure 3A). One possible explanation for the longer kinesin-1 ramp is that the catch-bond character of kinesin-1 engages at low loads rather than rising proportionally to load or engaging only near stall.

The most notable ramp behavior was seen in kinesin-3, where the ramp duration of 0.75 s was nearly four-fold shorter than the unloaded run duration (2.76 s) and was more than two-fold shorter than the stall duration (1.90 s) (Figure 3C, Table S1). As expanded on in the Discussion, the positively charged 'K-loop' in the kinesin-3 motor KIF1A is known to interact electrostatically with the negatively charged C-terminal tail of tubulin [54-56]; thus, it is reasonable that even the low loads imposed during ramps are sufficient to overcome these weak electrostatic interactions. The ramp duration is arguably the best definition of the time before KIF1A motors enter a partially dissociated 'slip' state, meaning that the observed unloaded durations represent a concatenation of multiple shorter runs interspersed by short diffusive events.

It was notable that the kinesin-3 stall durations at high load are longer than the ramp durations at low load, because this indicates that the kinesin-3 off-rate slows with increasing load. However, because kinesin-3 had the most slip events at stall, we were concerned that there may be undetected slip events below the 60 nm threshold of detection that led to an overestimation of the kinesin-3 stall duration. To test this hypothesis, we plotted the distribution of kinesin-3 slip distances at stall, fit an exponential, and calculated the fraction of missed slip events (Fig. S8). From this analysis, we calculated a correction factor of 1.42 that brought the kinesin-3 stall duration down 1.33 s. Notably, this stall duration value is still well above the kinesin-3 ramp duration value of 0.75 s in Fig. 3C and thus does not qualitatively change our conclusions.

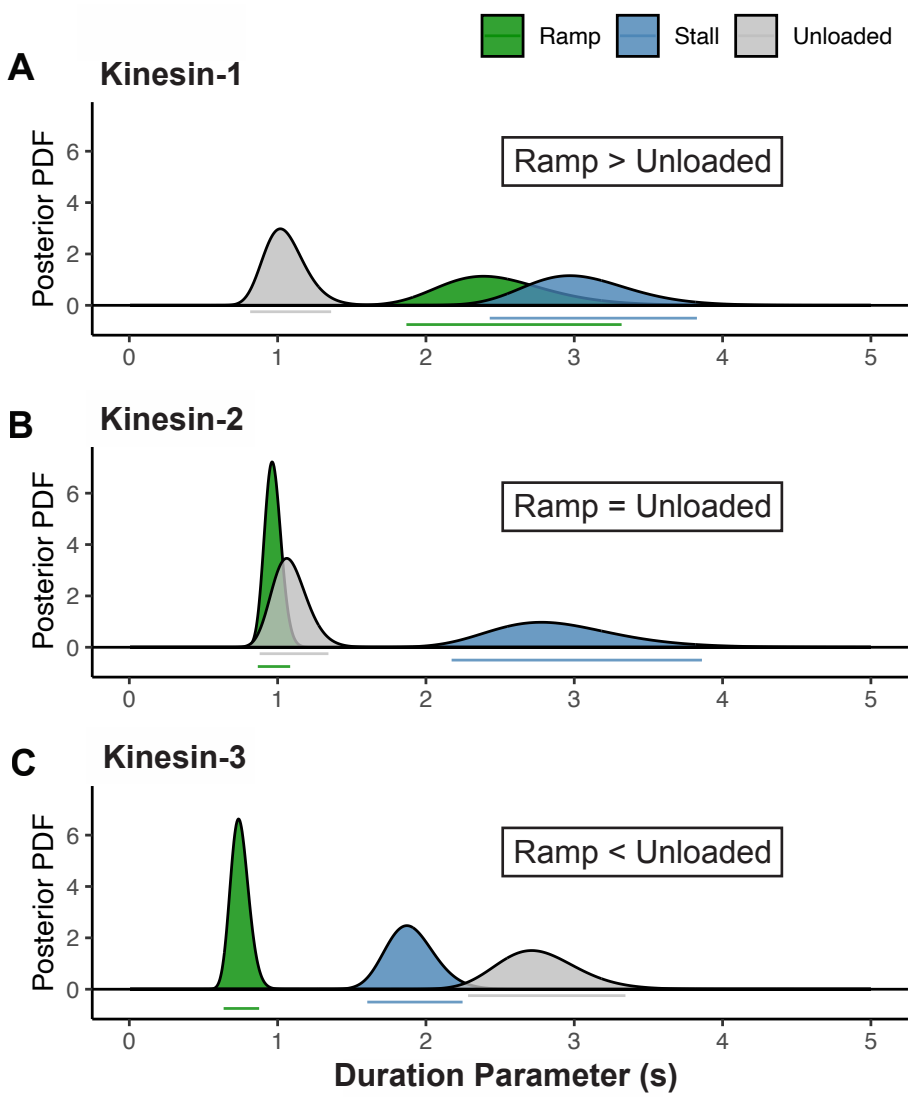

Figure 3. During Ramps, Kinesin-3 Detaches More Readily Than Under Zero Load. Unloaded, ramp, and stall duration parameters were estimated using a Markov process model, coupled with Bayesian inference methods. Curves show the posterior probability distributions of the duration parameters for (A) kinesin-1, (B) kinesin-2 and (C) kinesin-3. Bars below each peak indicate the 95% credible regions for the ramp (green), unloaded (gray) and stall (blue) duration parameters. Notably, the estimated ramp durations are larger, the same, and smaller than the unloaded run durations for kinesin-1, -2, and -3, respectively. For the unloaded and stall durations, this estimation method produces almost identical values as the maximum likelihood estimates in Figure 2 (values provided in Table S1).

Motor reengagement kinetics vary between families

Stall plateaus were terminated by three types of events: 1) small slips that initiated a new ramp, typically within a single frame (~40 ms), 2) the motor returning to the baseline and reengaging rapidly within a few frames (~100 msec), or 3) the motor returning to the baseline for a few seconds before reengaging (Figure 4A). We defined a slip event as a displacement of >60 nm from the plateau (distinguishable from normal small fluctuations at stall; Figure 1E) that recovers before reaching within 400 nm of the baseline (outside the range of normal baseline fluctuations; Figure 1F and S2). These

slip events have been observed previously for all three motor families in optical trapping experiments and are proposed to represent an intermediate state in which the motor exits the normal stepping cycle but remains associated with the microtubule [24,57-60]. As an initial analysis, we quantified the fraction of events for each motor (Figure 4A) and found that kinesin-3 had the highest proportion of slip events while kinesin-2 had the lowest proportion. In the context of pulling a large cargo through the viscous cytoplasm or competing against dynein in a tug-of-war, these slip events enable the motor to continue generating force after a small rearward displacement, rather than fully detaching and 'resetting' to zero load. Thus, we reanalyzed the stall durations for the three motors where slips are not counted and only disengagements where the motor returns to the baseline are counted as stall termination events (Figure 4B & C, Figure S7). By this definition, stall durations were between 1.5 and 3-fold longer for each motor, including kinesin-3.

To obtain a more complete picture of the motor reengagement kinetics for each motor, we plotted the time before starting a new ramp ($t_{restarting}$), including all slips and reattachments (Figure 4D-F). In each case, the distributions included a fast phase and a long tail of slower events. The distributions were fit with a tri-exponential function with the fast phase (30, 130 and 40 msec, respectively) accounting for roughly half of the events (Figure 4 D-F, Table S3). The fast population corresponds to slip and fast reattachment events classified in Figure 4A. The slower phases, which represent detachment events where the motor fluctuated around the baseline before initiating a new ramp, were the fastest for kinesin-3 (time constants of 0.15 and 1.34 s) and the slowest for kinesin-1 (time constants of 1.51 and 20.9 s). Interestingly, the order of the reattachment kinetics (kinesin-3 > kinesin-2 > kinesin-1) and the ~10-fold ratio of kinesin-3 to kinesin-1 match published bimolecular on-rate constants for microtubule binding from stopped-flow experiments (1.1, 4.6, and 17 μM-1 s-1 for kinesin-1,-2 and -3, respectively [56,61,62]).

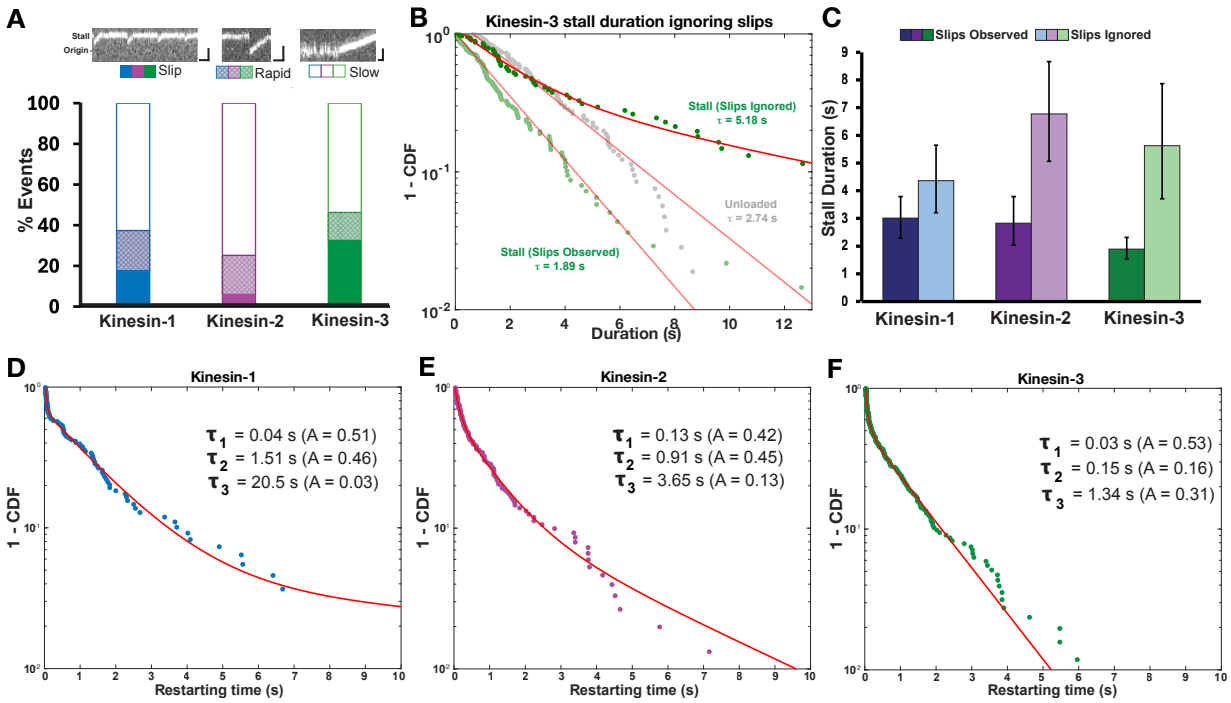

Figure 4. Restart Kinetics for Kinesin-1, -2 and -3. (A) Fraction of slip, fast rebinding, and slow rebinding events for each motor, with example kymographs for each (top; scale bars are 0.5 µm and 0.2 s). Solid colors indicate slips during stall, where the motor resumes a new ramp within a single frame (~40 ms), crosshatching indicates rapid reattachment events (100 ms) following fall to baseline, and open bars indicate slow reattachment events with >100 ms fluctuations around baseline. (B) Kinesin-3 stall durations, with unloaded run times in gray, stall durations terminated by slips in light green, and stall durations terminated by falling to the baseline (ignoring slips) in dark green. Unloaded and stall durations (replotted from Figure 2) were fit with single exponential functions in MEMLET. Stall durations ignoring slips were fit with a bi-exponential by least squares (τ_1 = 2.01 s [95% CI: 1.52, 2.35 s], A_1 = 0.66 s [0.54, 0.83 s], τ_2 = 11.0 s [9.18, 13.70], A_2 = 0.33 [0.23, 0.48]). Weighted average of the two time constants is displayed in plot for comparison to other time constants. Similar results for kinesin-1 and -2 are shown in Figure S7. (C) Comparison of stall durations for kinesins -1, -2 and -3 with slips observed as stall terminations or ignored. (D-F) Distribution of restart times for each motor fit to a tri-exponential (least squares). Confidence intervals of parameters determined by bootstrapping with 1000 iterations are given in Table S3.

Simulating Potential Catch-Bond Mechanisms

To compare the motor detachment and reattachment kinetics between the three kinesin transport families, we carried out stochastic simulations of load-dependent motor stepping, unbinding and rebinding. For simplicity, we reduced the chemomechanical cycle down to a single strongly-bound state (ATP and nucleotide-free states) and a single weakly-bound state (ADP and ADP-Pi states) (Figure 5A). Based on the published load and ATP dependencies of substeps in the kinesin-1 chemomechanical cycle [57], we incorporated a load-dependent strong-to-weak transition, $k_{s\text{-}w}$. Based on our restarting durations from Figure 4 and previous work [57-60], we included both a slip state, from which the motor recovers rapidly, and a detached state associated with a slower recovery. Runs or stalls are terminated by transition from the weakly-bound state into the slip state (k_{slip}). Based on backstepping rates observed in optical tweezer experiments, we incorporated a load-independent backward stepping

rate of 3 s^{-1}, meaning that stall is defined as the load at which forward stepping slows to 3 s^{-1} [63,64]. For simplicity, we set $k_{s-w} = k_{w-s}$ at zero load, meaning that the motor spends half of its cycle in each state, [65] with the rates set to match the unloaded velocity for each motor.

Using parameters chosen to match motor behavior under no load (Figure 5B), we were able to reproduce the unloaded run durations for all three motors, as expected (Figure 5C-E). Next, to match the experimental stall durations we incorporated a negative load dependence into the strong-to-weak transition rate (so that stepping slows with load) and a positive load dependence into the transition from the weakly-bound state into the slip state (so slipping occurs more frequently at higher loads). With these parameters (Figure 5B), we were able to reproduce the stall duration distribution for all three motors (Figure 5C-E). Importantly, in this model formulation, dissociation from the weakly-bound state acts as a slip-bond and the kinesin catch-bond characteristics are achieved by the motor spending a larger fraction of its cycle in the strongly-bound state under increasing loads.

To complete our model, we simulated recovery from the slip and detached states. The rate of rescue from the slip state (k_{resc}) was set based on the duration and relative amplitude of the fast phase of the restarting times in Figure 4. We posited that detachment follows the slip state, consistent with previous formulations [57,60]. The two slower restarting time constants from Figure 4 were used to set the reattachment rates, k_{reatt} (see Supplementary Methods for details). Using this approach, we were able to reproduce the restarting durations for all three motors (Figure 5F-H).

The rate constants derived from this model allow for a comparison of the specific transitions that differ between the three motor families. Three features are notable. First, for kinesin-3 the transition into the slip state at stall, k_{slip}, is the fastest of the three families, consistent with the observation by eye of the plateaus (Figure 1H and 4A) and consistent with previous three-bead optical trapping results [24]. Second, the rates of rescue from the slip state, k_{resc}, for the three motors match within a factor of two. Thus, the fast bimolecular on-rates from stopped flow and the relatively short durations before restarting we observe for kinesin-3 (Figure 4) do not result from a faster reengagement out of the slip state. Third, the slow reattachment rate for kinesin-3 is 10-fold faster than for kinesin-1 and -2. Hence, in this model formulation, both the fast bimolecular on-rates in solution[56] and short restart durations observed here for kinesin-3 result from recovery from a detached state rather than rescue from a slip state.

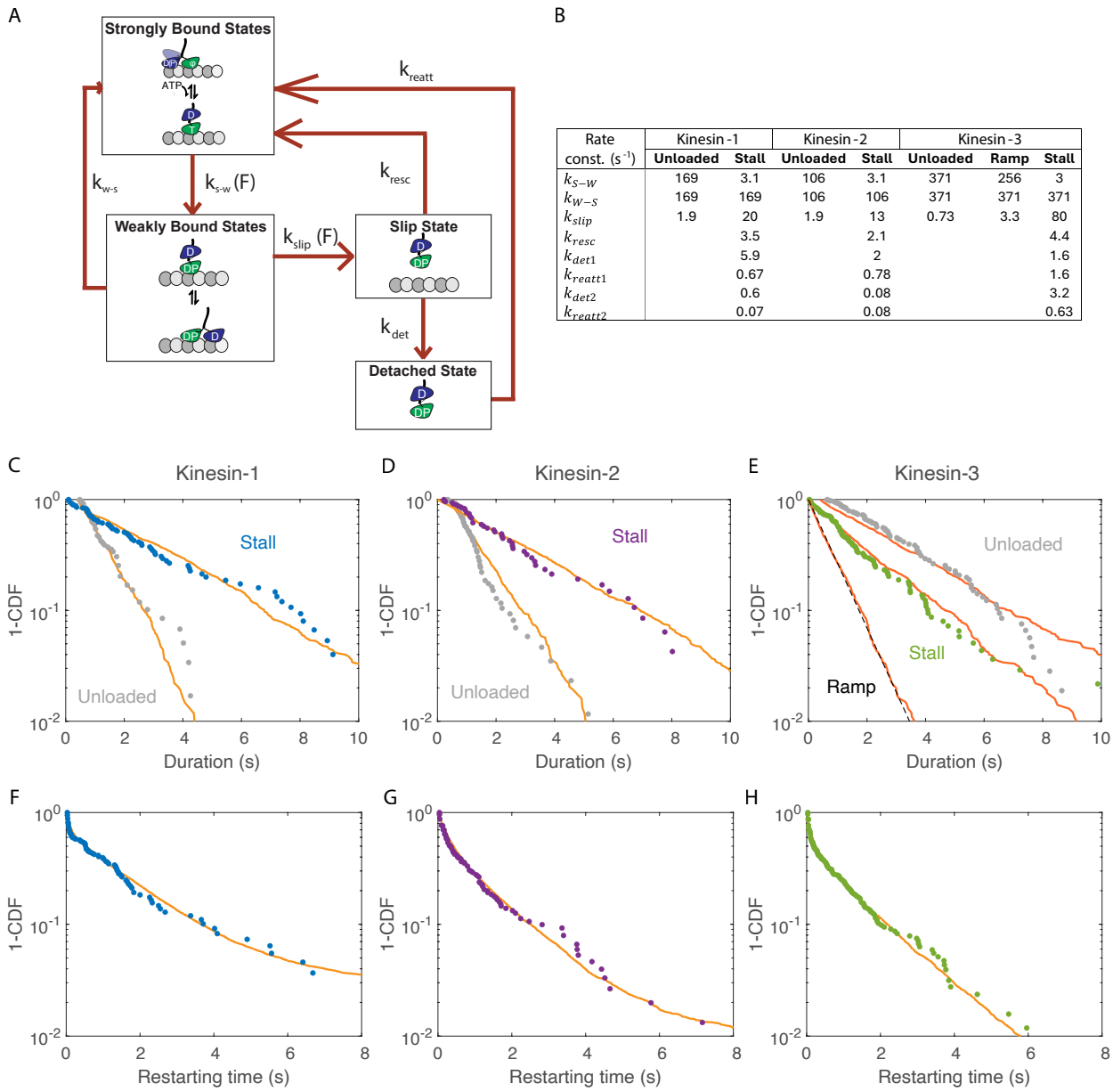

Rate const. (s^{-1})	Kinesin-1		Kinesin-2		Kinesin-3		
	Unloaded	Stall	Unloaded	Stall	Unloaded	Ramp	Stall
k_{S-W}	169	3.1	106	3.1	371	256	3
k_{W-S}	169	169	106	106	371	371	371
k_{slip}	1.9	20	1.9	13	0.73	3.3	80
k_{resc}		3.5		2.1			4.4
k_{det1}		5.9		2			1.6
k_{reatt1}		0.67		0.78			1.6
k_{det2}		0.6		0.08			3.2
k_{reatt2}		0.07		0.08			0.63

Figure 5. Chemomechanical Model of Proposed Catch-bond Mechanism. (A) Diagram of kinesin chemomechanical cycle model consisting of strongly- and weakly-bound states that make up the stepping cycle, and slip and detached states that terminate runs and stalls. Note that two pathways of detachment from the slip state (and reattachment) are incorporated into the model, but only one pathway is shown for simplicity (see Supplementary Methods for details). (B) Table of rate constants used to simulate unloaded and stall durations and restarting times. All rate constants are derived from fits to experimental data, as described in Supplemental Methods. $k_{S\text{-}W}$ and k_{slip} depended exponentially on load ($k(F) = k_0 e^{\frac{F\delta}{k_B T}}$) with δ for $k_{S\text{-}W}$ of -2.7, -2.4, and -3.6 nm and δ for k_{slip} of 1.6, 1.3 and 2.7 nm for kinesin-1, -2 and -3, respectively; see also Figure S9A). (C-E) Experimental (symbols) and simulated (lines) unloaded and stall durations. 10,000 events were simulated for each condition and plotted with minimum cutoffs matching experiments. Kinesin-3 ramp durations were taken from parameter estimated in Figure 3. (F-H) Experimental (symbols) and simulated (lines) restart times.

Discussion

Understanding how motors respond vectorially to external loads is crucial for understanding cargo transport in complex intracellular geometries and how kinesin motors compete against dynein in bidirectional transport [13,19]. Optical tweezer experiments have provided many essential details of the kinesin mechanochemical cycle under load; however, the bead diameters needed to achieve substantial trapping forces impose vertical forces on the motors. Using DNA as a nanospring enables mechanical experiments using a standard TIRF microscope and allows for simultaneous monitoring of numerous motor-DNA complexes in a single imaging field. With this geometry, a kinesin motor pulls against the elastic force of a stretched DNA nearly parallel to the microtubule, matching the geometry of vesicles measuring a few tens of nanometers. Similar approaches have been used to study myosin, dynein and kinesin-1 in both single-molecule and gliding assays [33-35,37,38,66,67]. The most striking observation was that members of all three kinesin transport families show catch-bond behavior in which off-rates at stall are slower than those at low or zero loads. Additionally, following disengagement from the microtubule, the three motor families reengaged with the microtubule with complex and family-specific kinetics.

Comparison to previous work

Despite the clear slip-bond behavior of kinesin-1 seen in single-bead optical traps, there has been growing evidence that kinesin-1 detachment is sensitive to the direction of load. Motor engagement times were shown to decrease when larger beads were employed in single-bead traps, and to be extended in geometries that minimize vertical forces such as the three-bead geometry or when a DNA tether was used [32,68]. In a study that employed DNA-tethered kinesin-1 to extract tubulin the microtubule lattice, pulling durations of ~30 s were observed at the lowest motor concentrations, indicative of kinesin-1 catch-bond behavior [33]. When kinesin-1 was connected to micron-scale beads through a DNA linker and hydrodynamic forces parallel to the microtubule imposed, dissociation rates were relatively insensitive to loads up to ~3 pN, inconsistent with slip-bond characteristics and instead characteristic of an ideal-bond [34]. The 3 s kinesin-1 stall duration in our tensiometer falls between the 30 s value for tubulin pulling and the 1.3 – 1.5 s engagement times measured in optical trap and hydrodynamic assays where vertical forces are minimized [32-34,68]. In contrast to kinesin-1, kinesin-3 (KIF1A) median engagement durations were found to be similarly short in both the one-bead (69 ms) and three bead (62 ms) optical trap geometries [24], much shorter than our 1.9 s stall duration in the DNA tensiometer. One difference may be that the millisecond temporal resolution in the optical tweezer enabled detection of many small slips that were undetected by our fluorescence approach; however, extrapolation of our measured kinesin-3 slip distances below our 60 nm detection limit (Fig. S8) argues against this. Secondly, the microtubule is held under tension in the three-bead experiment, which may alter the lattice properties. Finally, it can't be ruled out that KIF1A is particularly sensitive to vertical loads and small lateral or vertical forces present in the three-bead geometry are absent in the DNA tensiometer geometry. To date there have been no studies on kinesin-2 where vertical loads are minimized, and in single-bead optical traps the off-rate depends strongly on load[69].

Transport kinesins have a catch-bond behavior under hindering loads

What is the mechanism of the observed catch-bond behavior? Cell adhesion proteins such as integrins, selectins, and FimH have been shown to form longer lasting bonds under load, with the proposed mechanisms generally involving an allosteric effect that strengthens the protein:protein interface [70-72]. However, motor proteins are different in that they cycle in a nucleotide-dependent way between strongly- and weakly bound states, offering multiple potential mechanisms for slower dissociation rates under load. For instance, under a few piconewtons of load, Myosin I was shown to dissociate nearly two orders of magnitude slower than in the absence of load, an effect attributed to load-dependent trapping of ADP in the active site that maintained the motor a high-affinity binding state [73]. Dynein was also shown to have catch-bond behavior over certain ranges of resisting loads, though the precise mechanism is unclear [43,44,74,75].

We interpreted our stepping, detachment, and reattachment results using a model that incorporates a load-dependent strong-to-weak transition and a load-dependent entry into a transient 'slip' state preceding detachment. The key feature of the model is that under load the motor spends an increasing fraction of its hydrolysis cycle in a strongly-bound state that resists dissociation.

The role of vertical forces in motor detachment

We next asked whether by considering the different geometries we could reconcile our catch-bond observations with previous single-bead optical tweezer kinesin-1 slip-bond measurements that found the kinesin-1 off-rate increased from 1.11 s^{-1} at zero load to 2.67 s^{-1} at 6 pN [25]. Using a 440 nm bead diameter and estimated motor length of 35 nm that results in the force being imposed on the motor at a 60º angle (Figure S9B), a 6 pN stall force parallel to the microtubule corresponds to a 10 pN force perpendicular to the microtubule [25,31]. A model developed by Khataee and Howard was able to fully account for these geometry-dependent off-rates using a two-step detachment process having catch-bond behavior for parallel loads and slip-bond behavior for vertical loads [31]. Applying that model to our geometry and assuming a purely horizontal load and a 6 pN stall force, the predicted stall duration for kinesin-1 is 77 s, much longer than the 3 s we measure (Figure S9). We approached the detachment process differently, by incorporating a load-dependent transition in the hydrolysis cycle ($k_{S\text{-}W}$) and a load-dependent exit from the hydrolysis cycle (k_{slip}). To explore effects of vertical forces using our two-state model, we incorporated both horizontal and vertical loads as accelerating detachment from the weakly-bound state, as follows:

$$k_{slip}(F) = k_{slip}^{0} e^{\frac{(F_{\parallel}\delta_{\parallel} + F_{\perp}\delta_{\perp})}{k_B T}}$$

Here $F_{\parallel}$ and $F_{\perp}$ are the magnitude of the parallel and perpendicular loads and $\delta_{\parallel}$ and $\delta_{\perp}$ represent the distance parameters in each direction (Figure S9). Using $\delta_{\parallel}$ = 1.61 nm (Figure 5B), we found that by setting $\delta_{\perp}$ = 1.58 nm, we were able to reproduce the slip bond behavior observed in the single-bead optical trap experiments (Figure S9). Notably, this model implies that vertical and horizontal forces have similar effects on the transition rate into the slip state. We stress that this model is a hypothesis that needs further testing. Nonetheless, this is a simple formulation that shows that a motor can

display either catch bond or slip bond behavior depending on the geometry of the imposed loads.

Ramps reveal detachment behaviors at low loads

In addition to reporting on the detachment properties at stall, our DNA tensiometer provides new insights into fast rebinding that occurs during unloaded runs of kinesin-3. It has long been appreciated that the kinesin-3 motor KIF1A achieves long run lengths due to electrostatic attraction between its positively charged Loop-12 (K-loop) and the negatively charged C-terminal tail of tubulin [55,56,76-81]. Furthermore, the KIF1A off-rate in ADP, in which the motor diffuses on the microtubule lattice, was found to match the off-rate during processive stepping in ATP [56]. The relatively high microtubule affinity of this weakly-bound state suggests that the motor may be undergoing diffusive episodes between processive runs, while maintaining association with the microtubule.

Our DNA tensiometer offers a way to test the hypothesis that the long, unloaded run lengths of KIF1A are due to a concatenation of shorter runs. Due to the nonlinearity of the dsDNA force-extension curve in our DNA tensiometer, the motor is walking against forces below 1 pN for roughly 90% of the distance to stall (Figure 1B). Consistent with this, motor velocities before stall were nearly constant (Figure 1D and S3), and averaged ~15% slower than unloaded velocities (Table S2), which corresponds to ~1 pN of force if the force-velocity relationship is linear. Using a Bayesian Inference approach that takes into account motors that dissociate during the ramps as well as those that complete ramps by achieving stall, we measured a nearly four-fold faster KIF1A detachment rate during ramps than under zero load (Figure 3). If, under zero load, the long runs observed were actually a concatenation of a series of shorter runs connected by diffusive weakly-bound events, the diffusive state would likely be unable to withstand even the sub-pN forces from the DNA spring [80]. For instance, based on a 0.044 $\mu m^2/s$ diffusion coefficient (equivalent to a ~0.1 pN-s/μm drag coefficient [80,82]), if the motor were in a weakly-bound state for 10 ms, a 1 pN force would pull the motor back 100 nm. Thus, in considering whether KIF1A acts as a catch bond, we used this ramp duration as the best approximation for the true run unloaded length in the absence of diffusive events.

The ramp durations of kinesin-1 and kinesin-2 also provide insights into how load alters their interactions with microtubules. For kinesin-2, the predicted ramp duration was not statistically different from the unloaded run duration, suggesting that unloaded runs do not include short diffusive episodes. Interestingly the predicted ramp duration for kinesin-1 was nearly the same as the stall duration and much longer than the unloaded duration. One possibility is that the catch-bond effect of hindering load comes into play at low loads and not only at stall where the motor has slowed considerably.

Motor slips and detachments reflect different processes

Because the DNA tensiometer tethers the motor near the microtubule, such that repeated binding and unbinding events occur, it enables comparison of family-dependent differences in kinesin rebinding kinetics. In addition to clear detachment events, rapid slip and recovery events were observed for all three motors, with highest frequency for kinesin-3 and lowest frequency for kinesin-1. Backwards slipping while

maintaining association with the microtubule was first seen for kinesin-8 motors, which are highly processive yet generate only small forces [58]. Similar backward slips at stall were observed for kinesin-1, with kinetics that suggested a transition such as phosphate release precedes dissociation[60]. Subsequent higher resolution work, enabled by small Germanium nanoparticles, revealed a staircase pattern during these slips with ~8 nm steps of mean duration 73 μsec, suggesting that the motor was transiently interacting with each tubulin subunit as it slipped backward. Similar slips have also been observed for kinesin-2 and two kinesin-3 family members, KIF1A and KIF1C [24,59].

There is some dispute in the literature regarding the kinetics of kinesin-1 recovery from the slip state. Using a single-bead trap, Sudhakar found that 80% of restart events were slips with a time constant of 128 ms [57], whereas Toleikis measured slip recoveries that were essentially at the limit of detection (~1 ms) [60]. Using a three-bead trap, Pyrpassopoulis measured a 10 ms slip time constant for kinesin-1 [32]. Our 40 ms slip time constant, which accounts for half of recovery events, is limited by the camera frame rate, and thus is likely an overestimate. In the three-bead geometry, kinesin-3 (KIF1A) slips recovered with a time constant of 1 ms [24], faster than the 30 msec (upper limit estimate) we observe. Thus, the precise recovery rate is dependent on the detailed measurement and analysis used. In our DNA tensiometer results, the higher frequency of slips for kinesin-3 relative to kinesin-1 is seen by direct counting (Figure 4A), by the large enhanced stall duration when slips are not counted as termination events (Figure 4C), and by the fast k_{slip} parameter under load in the kinesin-3 model (Figure 5B).

Catch-bond behavior provides insights into tug-of-war with dynein

In previous simulations of kinesin-dynein bidirectional transport, we found that the strongest determinants of kinesin's ability to compete against dynein were the load-dependent motor dissociation rate and the motor rebinding rate [22,23]. Simply put, if motors detach, then the opposing motor wins. The finding here that all three dominant kinesin transport families display catch-bond like behavior at stall necessitates a reevaluation of how motors function during a tug-of-war. There is evidence that dynein forms a catch bond or at least an ideal (load independent) bond [14,43,44,74,75,83]; thus, kinesins and dyneins are primed to strongly oppose one another.

The catch bond results here help to explain previous in vitro work in which one kinesin and one dynein were connected through a complementary ssDNA [14,28,30]. It was found that the motor pairs had periods of near-zero velocity that lasted for many seconds, considerably longer than kinesin's unloaded off-rate. Furthermore, kinesin-2 and kinesin-3 also showed these sustained slow tug-of-war periods despite their reported faster load-dependent off-rates from optical tweezer studies. The functional catch-bond behavior observed here provides a simple explanation for these sustained kinesin-dynein stalemates.

Importantly, the load-dependent off-rates of both kinesins and dynein are expected to depend on the cargo geometry. A 30 nm vesicle would lead to forces on the motor nearly parallel to the microtubule surface, whereas when transporting a micron-scale mitochondria the vertical forces would be larger than the horizontal forces. Cargo geometry and stiffness are also expected to play a role; for instance, deformation of a cargo, either due to compliance of the cargo or to multiple motors pulling on it will tend

to reduce vertical force components on the motors. Additionally, any 'rolling' of a spherical cargo following motor detachment will tend to suppress the motor reattachment rate. The present work emphasizes that along with motor type, motor number, motor autoinhibition, and the growing list of regulatory proteins, the geometry with kinesin and dynein engage in a tug-of-war can be an important determinant of the speed and direction of cargo transport in cells.

Methods

DNA Tensiometer Construction

For the dsDNA spring, a 5' biotinylated forward primer (5'-/5Biosg/TGC CTC CGT GTA AGG GGG AT-3') and a reverse primer with a 5' overhang (5'-/GGG CCA TCG CCA ATT GGA GTA /idSp/ GTG AGT TAA AGT TGT ACT CGA GTT TGT GTC CAA GAA -3') were used to create a 3009 bp dsDNA by PCR from plasmid *Mus Musculus* BicD2-sf-GFP (aa 25-425) in pet28a. The abasic Int 1',2'-Dideoxyribose spacer (idSp) creates an overhang by terminating the polymerase. All oligonucleotides were purchased from IDT. Each 50 μL PCR reaction contained: 1x Phusion HF buffer, 198 μM dNTPs, 2 μM dCTP-Cy5, 0.5 μM primers, 3 ng template DNA and 1 U/50 μL HF Phusion Polymerase. Fluorescent dsDNA used in Figure S4 had 10 μM dCTP-Cy5 and 190 μM dNTPs. The PCR reaction was carried out in a thermal cycler with the following procedure: 98℃ for 30 s, then 45 cycles of 98℃ for 10 s, 58℃ for 30 s and 72℃ for 1.5 min, then lastly 72℃ for 5 min. The product was purified using a NucleoSpin® PCR clean-up kit and the concentration determined by absorbance on a Nanodrop 2000c Spectrophotometer. DNA bands were visualized on a 1% agarose gel with ethidium bromide staining.

Motor-Microtubule-Tensiometer Assembly

Motors were bacterially expressed, purified and linked through its SNAP tag to an oligonucleotide (5'-/TAC TCC AAT TGG CGA TGG CCC / 3AmMC6T/-3') complementary to the dsDNA overhang. Details of motor expression, purification and labeling, as well as tubulin biotinylation and polymerization are given in Supplementary Information. The DNA tensiometer was assembled on the microtubule as follows. The following three buffers are made on the same day of the experiment: C2AT (BRB80, 10 μM Taxol, 2 mM MgATP, 2 mg/mL Casein), 2AT (BRB80, 10 μM Taxol, 2 mM MgATP) and Imaging Solution (BRB80, 10 μM Taxol, 2 mg/mL Casein, 2 mM MgATP, 20 mM D-glucose, 0.02 mg/mL Glucose oxidase, 0.008 mg/mL Catalase, 0.5% BME and 2 mg/mL BSA). Full-length rigor kinesin was used to attach microtubules to the coverglass [65]. Tensiometers were created in the flow cell using the following work flow: C2AT, 5 min > Rigor kinesin, 5 min> C2AT wash > BioMT, 5 min > 2AT > 8 nM Neutravidin, 5 min> 2AT > 10 nM Bio-dsDNA-Overhang, 5 min> C2AT > 4 nM KinesinMotor + 40nM Qdot-GBP (pre incubated in tube on ice for >15 min) in imaging solution, 10 min > Imaging solution wash. Note that because casein can contain free biotin, casein-free 2AT buffer was used during avidin-biotin binding steps. Following assembly, the Qdot connected to the motor was imaged on a custom-built TIRF microscope, described previously [84]. Raw data were typically collected at 25 fps (range of 20-40 fps) on a Photometrics Prime 95B camera.

Data Analysis

Movies were uploaded into FIESTA software [85] and Qdot intensities were tracked using a symmetric 2-D gaussian function to obtain x,y,t data for each Qdot. When drift correction was needed, TetraSpeck™ Fluorescent Microspheres (Thermo) and immobile Qdots were used as fiducial markers. The smallest position errors at stall in FIESTA fitting were 3-4 nm, which matched the positional error of Qdot-labeled motors stuck to microtubules in AMPPNP. Points with position errors greater than 20 nm were excluded because they often involved clearly spurrious position estimates. Notably, many tensiometers had small segments of missing data due to the Qdot fluctuating out of the TIRF field or blinking; these occurred most often during periods when the motors were detached from the microtubule.

After obtaining X and Y positions of linear motor tracks in Fiesta, we rotated and translated the data in Excel to generate X versus t traces. The apparent origin was determined by averaging the points where the motor is fluctuating on its tether. In rare instances where no fluctuation was observed, the approximate origin was calculated by averaging the starting positions of all the ramps within the tensiometer (Figure 1). We then measured the ramp time, distance traveled, stall durations, reattachment times and starting positions. Tensiometers occasionally ended with the Qdot signal going dark, denoting either bleaching or failure of the Qdot-motor or motor-DNA connection. Notably, no clear instances of motor-Qdots walking past the plateau point (denoting the tensiometer breaking) were observed. Stalls that terminated due to the tensiometer going dark or the video ending were excluded from analysis.

Stochastic Modeling

Kinesin run and stall durations were simulated by using a modified version of published stochastic model of kinesin stepping [23,30]. A motor is either in a strongly-bound state or a weakly-bound state (Figure 5A). At each timepoint, a motor in the strongly bound state can transition into the weakly-bound state with a first order transition rate constant, k_{S-W} or step backward by 8 nm with a constant rate, $k_{back} = 3\ s^{-1}$. A motor in the weakly-bound state can complete an 8-nm forward step by transitioning back to the strongly-bound state with rate constant, k_{W-S}, or it can disengage from the microtubule with transition rate, k_{slip}.

For simplicity, we set $k_{S-W} = k_{W-S}$ at zero load. Load-dependent transition rates were defined as:

$$k(F) = k^0 * e^{\frac{F\delta}{k_B T}}$$

where k^0 is the unloaded transition rate, δ is the characteristic distance parameter and $k_B T$ is the Boltzmann's constant multiplied by the absolute temperature, equal to 4.1 pN-nm at $25°$ C. Stall force was set to 6 pN. Unloaded and stall durations were simulated by starting the motor in strongly-bound state and continuing until it transitioned into the slip state, with 1000 simulations for each condition. Restart times were simulated by starting the motor in the slip state. From there, the motor can reengage by transitioning into the strongly-bound state or switch to one of two detached states having either a slow or fast recovery rate. Restart simulations were run for 10,000

iterations. Model parameters were constrained by experimental data, described fully in Supplementary Methods.

Acknowledgments

This work was originally conceived as part of a NIH-funded collaborative modeling project to Will Hancock, Scott McKinley, John Fricks, and Peter Kramer (R01GM122082). We thank Qingzhou Feng, Scott Pflumm, and Adheshwari Ramesh for early efforts on this project and all members of the Hancock Lab for helpful discussions. This work was funded by NIH Grant R35GM139568 to W.O.H.. C.R.N. was supported by NIH postdoctoral fellowship F32GM149114, R.J. was supported by NIH Training Grant T32GM108563, and S.A.M. was supported by the NSF-Simons Southeast Center for Mathematics and Biology (SCMB) through grant NSF-DMS1764406 and Simons Foundation-SFARI 594594.

References

1 Millecamps, S. & Julien, J. P. Axonal transport deficits and neurodegenerative diseases. *Nat Rev Neurosci* **14**, 161-176 (2013). https://doi.org:10.1038/nrn3380

2 Brenner, D. *et al.* Hot-spot KIF5A mutations cause familial ALS. *Brain* **141**, 688-697 (2018). https://doi.org:10.1093/brain/awx370

3 Caballero Oteyza, A. *et al.* Motor protein mutations cause a new form of hereditary spastic paraplegia. *Neurology* **82**, 2007-2016 (2014). https://doi.org:10.1212/WNL.0000000000000479

4 Makrythanasis, P. *et al.* Biallelic variants in KIF14 cause intellectual disability with microcephaly. *Eur J Hum Genet* **26**, 330-339 (2018). https://doi.org:10.1038/s41431-017-0088-9

5 Moawia, A. *et al.* Mutations of KIF14 cause primary microcephaly by impairing cytokinesis. *Ann Neurol* **82**, 562-577 (2017). https://doi.org:10.1002/ana.25044

6 Pant, D. C. *et al.* ALS-linked KIF5A DeltaExon27 mutant causes neuronal toxicity through gain-of-function. *EMBO Rep* **23**, e54234 (2022). https://doi.org:10.15252/embr.202154234

7 Reid, E. *et al.* A kinesin heavy chain (KIF5A) mutation in hereditary spastic paraplegia (SPG10). *Am J Hum Genet* **71**, 1189-1194 (2002). https://doi.org:10.1086/344210

8 Zhou, Y. *et al.* Loss-of-function of kinesin-5 KIF11 causes microcephaly, chorioretinopathy, and developmental disorders through chromosome instability and cell cycle arrest. *Exp Cell Res* **436**, 113975 (2024). https://doi.org:10.1016/j.yexcr.2024.113975

9 Hendricks, A. G. *et al.* Motor coordination via a tug-of-war mechanism drives bidirectional vesicle transport. *Curr Biol* **20**, 697-702 (2010). https://doi.org:10.1016/j.cub.2010.02.058

10 Welte, M. A. Bidirectional transport along microtubules. *Curr Biol* **14**, R525-537 (2004). https://doi.org:10.1016/j.cub.2004.06.045

11 Soppina, V., Rai, A. K., Ramaiya, A. J., Barak, P. & Mallik, R. Tug-of-war between dissimilar teams of microtubule motors regulates transport and fission of endosomes. *Proc Natl Acad Sci U S A* **106**, 19381-19386 (2009). https://doi.org:10.1073/pnas.0906524106
12 Encalada, S. E., Szpankowski, L., Xia, C. H. & Goldstein, L. S. Stable kinesin and dynein assemblies drive the axonal transport of mammalian prion protein vesicles. *Cell* **144**, 551-565 (2011). https://doi.org:10.1016/j.cell.2011.01.021
13 Hancock, W. O. Bidirectional cargo transport: moving beyond tug of war. *Nat Rev Mol Cell Biol* **15**, 615-628 (2014). https://doi.org:10.1038/nrm3853
14 Belyy, V. *et al.* The mammalian dynein-dynactin complex is a strong opponent to kinesin in a tug-of-war competition. *Nat Cell Biol* **18**, 1018-1024 (2016). https://doi.org:10.1038/ncb3393
15 Muller, M. J., Klumpp, S. & Lipowsky, R. Tug-of-war as a cooperative mechanism for bidirectional cargo transport by molecular motors. *Proc Natl Acad Sci U S A* **105**, 4609-4614 (2008). https://doi.org:10.1073/pnas.0706825105
16 Gross, S. P. Hither and yon: a review of bi-directional microtubule-based transport. *Phys Biol* **1**, R1-11 (2004). https://doi.org:10.1088/1478-3967/1/2/R01
17 Derr, N. D. *et al.* Tug-of-war in motor protein ensembles revealed with a programmable DNA origami scaffold. *Science* **338**, 662-665 (2012). https://doi.org:10.1126/science.1226734
18 Yildiz, A. Mechanism and regulation of kinesin motors. *Nat Rev Mol Cell Biol* **26**, 86-103 (2025). https://doi.org:10.1038/s41580-024-00780-6
19 Cason, S. E. & Holzbaur, E. L. F. Selective motor activation in organelle transport along axons. *Nat Rev Mol Cell Biol* **23**, 699-714 (2022). https://doi.org:10.1038/s41580-022-00491-w
20 Reck-Peterson, S. L., Redwine, W. B., Vale, R. D. & Carter, A. P. The cytoplasmic dynein transport machinery and its many cargoes. *Nat Rev Mol Cell Biol* **19**, 382-398 (2018). https://doi.org:10.1038/s41580-018-0004-3
21 D'Souza, A. I., Grover, R., Monzon, G. A., Santen, L. & Diez, S. Publisher Correction: Vesicles driven by dynein and kinesin exhibit directional reversals without regulators. *Nat Commun* **15**, 736 (2024). https://doi.org:10.1038/s41467-024-45256-5
22 Ohashi, K. G. *et al.* Load-dependent detachment kinetics plays a key role in bidirectional cargo transport by kinesin and dynein. *Traffic* **20**, 284-294 (2019). https://doi.org:10.1111/tra.12639
23 Ma, T. C., Gicking, A. M., Feng, Q. & Hancock, W. O. Simulations suggest robust microtubule attachment of kinesin and dynein in antagonistic pairs. *Biophys J* **122**, 3299-3313 (2023). https://doi.org:10.1016/j.bpj.2023.07.007
24 Pyrpassopoulos, S., Gicking, A. M., Zaniewski, T. M., Hancock, W. O. & Ostap, E. M. KIF1A is kinetically tuned to be a superengaging motor under hindering loads. *Proc Natl Acad Sci U S A* **120**, e2216903120 (2023). https://doi.org:10.1073/pnas.2216903120
25 Andreasson, J. O. *et al.* Examining kinesin processivity within a general gating framework. *Elife* **4** (2015). https://doi.org:10.7554/eLife.07403

26 Tomishige, M., Klopfenstein, D. R. & Vale, R. D. Conversion of Unc104/KIF1A kinesin into a processive motor after dimerization. *Science* **297**, 2263-2267 (2002). https://doi.org:10.1126/science.1073386
27 Budaitis, B. G. *et al.* Pathogenic mutations in the kinesin-3 motor KIF1A diminish force generation and movement through allosteric mechanisms. *J Cell Biol* **220** (2021). https://doi.org:10.1083/jcb.202004227
28 Feng, Q., Gicking, A. M. & Hancock, W. O. Dynactin p150 promotes processive motility of DDB complexes by minimizing diffusional behavior of dynein. *Mol Biol Cell* **31**, 782-792 (2020). https://doi.org:10.1091/mbc.E19-09-0495
29 Yildiz, A., Tomishige, M., Gennerich, A. & Vale, R. D. Intramolecular strain coordinates kinesin stepping behavior along microtubules. *Cell* **134**, 1030-1041 (2008). https://doi.org:10.1016/j.cell.2008.07.018
30 Gicking, A. M. *et al.* Kinesin-1, -2, and -3 motors use family-specific mechanochemical strategies to effectively compete with dynein during bidirectional transport. *Elife* **11** (2022). https://doi.org:10.7554/eLife.82228
31 Khataee, H. & Howard, J. Force Generated by Two Kinesin Motors Depends on the Load Direction and Intermolecular Coupling. *Phys Rev Lett* **122**, 188101 (2019). https://doi.org:10.1103/PhysRevLett.122.188101
32 Pyrpassopoulos, S., Shuman, H. & Ostap, E. M. Modulation of Kinesin's Load-Bearing Capacity by Force Geometry and the Microtubule Track. *Biophys J* **118**, 243-253 (2020). https://doi.org:10.1016/j.bpj.2019.10.045
33 Kuo, Y. W., Mahamdeh, M., Tuna, Y. & Howard, J. The force required to remove tubulin from the microtubule lattice by pulling on its alpha-tubulin C-terminal tail. *Nat Commun* **13**, 3651 (2022). https://doi.org:10.1038/s41467-022-31069-x
34 Urbanska, M. *et al.* Highly-Parallel Microfluidics-Based Force Spectroscopy on Single Cytoskeletal Motors. *Small* **17**, e2007388 (2021). https://doi.org:10.1002/smll.202007388
35 Iwaki, M., Wickham, S. F., Ikezaki, K., Yanagida, T. & Shih, W. M. A programmable DNA origami nanospring that reveals force-induced adjacent binding of myosin VI heads. *Nat Commun* **7**, 13715 (2016). https://doi.org:10.1038/ncomms13715
36 Marko, J. F. & Siggia, E. D. Stretching DNA. *Macromolecules* **28**, 8759-8770 (1995).
37 Shukla, S. *et al.* High-throughput force measurement of individual kinesin-1 motors during multi-motor transport. *Nanoscale* **14**, 12463-12475 (2022). https://doi.org:10.1039/d2nr01701f
38 Diez, S. *et al.* Stretching and Transporting DNA Molecules Using Motor Proteins. *Nano Lett* **3**, 1251-1254 (2003).
39 Thomas, W. E., Vogel, V. & Sokurenko, E. Biophysics of catch bonds. *Annu Rev Biophys* **37**, 399-416 (2008). https://doi.org:10.1146/annurev.biophys.37.032807.125804
40 Schnitzer, M. J., Visscher, K. & Block, S. M. Force production by single kinesin motors. *Nat Cell Biol* **2**, 718-723 (2000). https://doi.org:10.1038/35036345
41 Bell, G. I. Models for the specific adhesion of cells to cells. *Science* **200**, 618-627 (1978). https://doi.org:10.1126/science.347575

42 Rao, L. & Gennerich, A. Single-Molecule Studies on the Motion and Force Generation of the Kinesin-3 Motor KIF1A. *Methods Mol Biol* **2478**, 585-608 (2022). https://doi.org:10.1007/978-1-0716-2229-2_21
43 Kunwar, A. *et al.* Mechanical stochastic tug-of-war models cannot explain bidirectional lipid-droplet transport. *Proc Natl Acad Sci U S A* **108**, 18960-18965 (2011). https://doi.org:10.1073/pnas.1107841108
44 Rai, A. K., Rai, A., Ramaiya, A. J., Jha, R. & Mallik, R. Molecular adaptations allow dynein to generate large collective forces inside cells. *Cell* **152**, 172-182 (2013). https://doi.org:10.1016/j.cell.2012.11.044
45 Ezber, Y., Belyy, V., Can, S. & Yildiz, A. Dynein Harnesses Active Fluctuations of Microtubules for Faster Movement. *Nat Phys* **16**, 312-316 (2020). https://doi.org:10.1038/s41567-019-0757-4
46 Rao, L., Berger, F., Nicholas, M. P. & Gennerich, A. Molecular mechanism of cytoplasmic dynein tension sensing. *Nat Commun* **10**, 3332 (2019). https://doi.org:10.1038/s41467-019-11231-8
47 Blehm, B. H., Schroer, T. A., Trybus, K. M., Chemla, Y. R. & Selvin, P. R. In vivo optical trapping indicates kinesin's stall force is reduced by dynein during intracellular transport. *Proc Natl Acad Sci U S A* **110**, 3381-3386 (2013). https://doi.org:10.1073/pnas.1219961110
48 Svoboda, K. & Block, S. M. Force and velocity measured for single kinesin molecules. *Cell* **77**, 773-784 (1994). https://doi.org:10.1016/0092-8674(94)90060-4
49 Visscher, K., Schnitzer, M. J. & Block, S. M. Single kinesin molecules studied with a molecular force clamp. *Nature* **400**, 184-189 (1999). https://doi.org:10.1038/22146
50 Kojima, H., Muto, E., Higuchi, H. & Yanagida, T. Mechanics of single kinesin molecules measured by optical trapping nanometry. *Biophys J* **73**, 2012-2022 (1997). https://doi.org:10.1016/S0006-3495(97)78231-6
51 Schroeder, H. W., 3rd *et al.* Force-dependent detachment of kinesin-2 biases track switching at cytoskeletal filament intersections. *Biophys J* **103**, 48-58 (2012). https://doi.org:10.1016/j.bpj.2012.05.037
52 Woody, M. S., Lewis, J. H., Greenberg, M. J., Goldman, Y. E. & Ostap, E. M. MEMLET: An Easy-to-Use Tool for Data Fitting and Model Comparison Using Maximum-Likelihood Estimation. *Biophys J* **111**, 273-282 (2016). https://doi.org:10.1016/j.bpj.2016.06.019
53 Block, S. M., Goldstein, L. S. & Schnapp, B. J. Bead movement by single kinesin molecules studied with optical tweezers. *Nature* **348**, 348-352 (1990).
54 Soppina, P. *et al.* Kinesin-3 motors are fine-tuned at the molecular level to endow distinct mechanical outputs. *BMC Biol* **20**, 177 (2022). https://doi.org:10.1186/s12915-022-01370-8
55 Zaniewski, T. M. & Hancock, W. O. Positive charge in the K-loop of the kinesin-3 motor KIF1A regulates superprocessivity by enhancing microtubule affinity in the one-head-bound state. *J Biol Chem* **299**, 102818 (2023). https://doi.org:10.1016/j.jbc.2022.102818
56 Zaniewski, T. M., Gicking, A. M., Fricks, J. & Hancock, W. O. A kinetic dissection of the fast and superprocessive kinesin-3 KIF1A reveals a predominant one-

head-bound state during its chemomechanical cycle. *J Biol Chem* **295**, 17889-17903 (2020). https://doi.org:10.1074/jbc.RA120.014961
57 Sudhakar, S. *et al.* Germanium nanospheres for ultraresolution picotensiometry of kinesin motors. *Science* **371** (2021). https://doi.org:10.1126/science.abd9944
58 Jannasch, A., Bormuth, V., Storch, M., Howard, J. & Schaffer, E. Kinesin-8 is a low-force motor protein with a weakly bound slip state. *Biophys J* **104**, 2456-2464 (2013). https://doi.org:10.1016/j.bpj.2013.02.040
59 Siddiqui, N. *et al.* Force generation of KIF1C is impaired by pathogenic mutations. *Curr Biol* **32**, 3862-3870 e3866 (2022). https://doi.org:10.1016/j.cub.2022.07.029
60 Toleikis, A., Carter, N. J. & Cross, R. A. Backstepping Mechanism of Kinesin-1. *Biophys J* **119**, 1984-1994 (2020). https://doi.org:10.1016/j.bpj.2020.09.034
61 Chen, G. Y., Arginteanu, D. F. & Hancock, W. O. Processivity of the kinesin-2 KIF3A results from rear head gating and not front head gating. *J Biol Chem* **290**, 10274-10294 (2015). https://doi.org:10.1074/jbc.M114.628032
62 Feng, Q., Mickolajczyk, K. J., Chen, G. Y. & Hancock, W. O. Motor Reattachment Kinetics Play a Dominant Role in Multimotor-Driven Cargo Transport. *Biophys J* **114**, 400-409 (2018). https://doi.org:10.1016/j.bpj.2017.11.016
63 Coppin, C. M., Pierce, D. W., Hsu, L. & Vale, R. D. The load dependence of kinesin's mechanical cycle. *Proc Natl Acad Sci U S A* **94**, 8539-8544 (1997). https://doi.org:10.1073/pnas.94.16.8539
64 Carter, N. J. & Cross, R. A. Mechanics of the kinesin step. *Nature* **435**, 308-312 (2005). https://doi.org:10.1038/nature03528
65 Mickolajczyk, K. J. *et al.* Kinetics of nucleotide-dependent structural transitions in the kinesin-1 hydrolysis cycle. *Proc Natl Acad Sci U S A* **112**, E7186-7193 (2015). https://doi.org:10.1073/pnas.1517638112
66 Nick Maleki, A., Huis In 't Veld, P. J., Akhmanova, A., Dogterom, M. & Volkov, V. A. Estimation of microtubule-generated forces using a DNA origami nanospring. *J Cell Sci* **136** (2023). https://doi.org:10.1242/jcs.260154
67 Takamatsu, N., Furumoto, H., Ariga, T., Iwaki, M. & Hayashi, K. Stall force measurement of the kinesin-3 motor KIF1A using a programmable DNA origami nanospring. *bioRxiv*, 2025.2007.2002.662715 (2025). https://doi.org:10.1101/2025.07.02.662715
68 Hensley, A. M. & Yildiz, A. Enhanced Processivity and Collective Force Production of Kinesin-1 at Low Radial Forces. *bioRxiv* (2025). https://doi.org:10.1101/2025.08.27.672644
69 Andreasson, J. O., Shastry, S., Hancock, W. O. & Block, S. M. The Mechanochemical Cycle of Mammalian Kinesin-2 KIF3A/B under Load. *Curr Biol* **25**, 1166-1175 (2015). https://doi.org:10.1016/j.cub.2015.03.013
70 Kong, F., Garcia, A. J., Mould, A. P., Humphries, M. J. & Zhu, C. Demonstration of catch bonds between an integrin and its ligand. *J Cell Biol* **185**, 1275-1284 (2009). https://doi.org:10.1083/jcb.200810002
71 Marshall, B. T. *et al.* Direct observation of catch bonds involving cell-adhesion molecules. *Nature* **423**, 190-193 (2003). https://doi.org:10.1038/nature01605

72 Thomas, W. E., Trintchina, E., Forero, M., Vogel, V. & Sokurenko, E. V. Bacterial adhesion to target cells enhanced by shear force. *Cell* **109**, 913-923 (2002). https://doi.org:10.1016/s0092-8674(02)00796-1
73 Laakso, J. M., Lewis, J. H., Shuman, H. & Ostap, E. M. Myosin I can act as a molecular force sensor. *Science* **321**, 133-136 (2008). https://doi.org:10.1126/science.1159419
74 Rai, A. *et al.* Dynein Clusters into Lipid Microdomains on Phagosomes to Drive Rapid Transport toward Lysosomes. *Cell* **164**, 722-734 (2016). https://doi.org:10.1016/j.cell.2015.12.054
75 Sanghavi, P., Kumar, P., Roy, A., Madhusudhan, M. S. & Mallik, R. On and off controls within dynein-dynactin on native cargoes. *Proc Natl Acad Sci U S A* **118** (2021). https://doi.org:10.1073/pnas.2103383118
76 Soppina, V. *et al.* Dimerization of mammalian kinesin-3 motors results in superprocessive motion. *Proc Natl Acad Sci U S A* **111**, 5562-5567 (2014). https://doi.org:10.1073/pnas.1400759111
77 Soppina, V. & Verhey, K. J. The family-specific K-loop influences the microtubule on-rate but not the superprocessivity of kinesin-3 motors. *Mol Biol Cell* **25**, 2161-2170 (2014). https://doi.org:10.1091/mbc.E14-01-0696
78 Lessard, D. V. *et al.* Polyglutamylation of tubulin's C-terminal tail controls pausing and motility of kinesin-3 family member KIF1A. *J Biol Chem* **294**, 6353-6363 (2019). https://doi.org:10.1074/jbc.RA118.005765
79 Okada, Y. & Hirokawa, N. A processive single-headed motor: kinesin superfamily protein KIF1A. *Science* **283**, 1152-1157 (1999). https://doi.org:10.1126/science.283.5405.1152
80 Okada, Y. & Hirokawa, N. Mechanism of the single-headed processivity: diffusional anchoring between the K-loop of kinesin and the C terminus of tubulin. *Proc Natl Acad Sci U S A* **97**, 640-645 (2000). https://doi.org:10.1073/pnas.97.2.640
81 Okada, Y., Higuchi, H. & Hirokawa, N. Processivity of the single-headed kinesin KIF1A through biased binding to tubulin. *Nature* **424**, 574-577 (2003). https://doi.org:10.1038/nature01804
82 Howard, J. *Mechanics of Motor Proteins and the Cytoskeleton*. (Sinauer Associates, 2001).
83 Cianfrocco, M. A., DeSantis, M. E., Leschziner, A. E. & Reck-Peterson, S. L. Mechanism and regulation of cytoplasmic dynein. *Annu Rev Cell Dev Biol* **31**, 83-108 (2015). https://doi.org:10.1146/annurev-cellbio-100814-125438
84 Nong, D. *et al.* Integrated multi-wavelength microscope combining TIRFM and IRM modalities for imaging cellulases and other processive enzymes. *Biomed Opt Express* **12**, 3253-3264 (2021). https://doi.org:10.1364/BOE.423798
85 Ruhnow, F., Zwicker, D. & Diez, S. Tracking single particles and elongated filaments with nanometer precision. *Biophys J* **100**, 2820-2828 (2011). https://doi.org:10.1016/j.bpj.2011.04.023